An optical tool to optimize the output of a photonic integrated chip architecture

Luca Gemma, Martino Bernard, Davide Brunelli *Senior member, IEEE*

***Abstract*—Photonic Integrated Chips (PICs) are an up-and-coming solution for base building blocks of quantum computers. The ready accessibility of photonics integrated systems and the fact that they allow for direct monolithic integration with electronics in a compact architecture have pushed the academic community to inspect their capabilities further. Still, at this stage, their characterization, control, and fine-tuning is an open issue for which this work aims to provide a viable solution. In this paper we present a method for an easy setup and an efficient architecture to simultaneously optimize multiple outputs of a PIC. The proposed solution can be embedded in an automation tool for tuning and verifying output on- and off-chip detectors. We fabricated a Silicon Oxynitride (SiON)-based PIC featuring a network of Mach-Zehnder interferometers (MZI) arranged in Clements architecture driven by Titanium-Titanium Nitride (TiTiN) thermistors. We interfaced the chip electronically through commercial driver modules and optically through optical guides and controlled it through a Python optimization algorithm. Finally, we retrieved the feedback of the control both by sensing it through integrated silicon photodetectors and by an image processing algorithm capable of inspecting the light intensity scattered by the waveguides in a custom region.**

***Index Terms*—quantum circuits, PIC, Image processing, optimization algorithm**

I. Introduction

QUANTUM computing is a promising game-breaking technology largely under the scientific community's focus. Quantum states can be theoretically achieved and exploited through different processes like superconducting circuits (Rigetti and IBM), topological systems (Microsoft), Photonic Systems (PsiQuantum), trapped ions (IonQ), and quantum annealing (DWave). Rigetti's work on superconducting caps [1] shows the fabrication of such critical elements when dealing with isolation, vacuum, and resonant elements. IBM illustrates in [2] the complex design of superconducting quantum circuits following a quasi-lumped model approach. Microsoft illustrates in [3] a slid fault-tolerant quantum computing approach with semiconducting nanowires regarding topological systems. PsiQuantum and Mercedes-Benz R&D show in [4] how fault-tolerant quantum computing can really contribute to battery design using silicon photonics as a quantum technology enabler. IonQ discusses in [5] about the optimization of power consumption of two-qubit gates, presenting a new optimization principle for such basic quantum elements, especially making references to trapped-ion quantum computers. DWave states in [6] several major architectural deliberations when dealing with the design of a superconducting quantum annealing processor. QuiX Quantum shows the largest photonic quantum processor [7] by illustrating a 20 input-outputs mode architecture based on reconfigurable interferometers. Lastly, the debate over quantum solutions is yet to be closed, with societies such as Xanadu [8] that questions about how today's literature should focus and provide ways to benchmark quantum computing progresses and applications such as quantum machine learning.

In the present work, we will discuss silicon photonics as our enabling technology as it is a mature technology that has several advantages over its alternatives when considering established technologies and facilities we had access to. First, integrated photonics is the natural candidate interface with current classical telecommunications technologies. In addition, photonic chips for quantum technologies are scalable as, for example, they do not require hard cooling as superconducting circuits do. Lastly, the fabrication techniques are borrowed from those of Very Large Scale Integrated (VLSI) circuits; thus, they can be fabricated monotonically together with an electronic circuit with relatively low overhead. Therefore, PICs can potentially open seamless interactions with standard electronics, embedding the photonics and electronics in a compact solution.

The typical implementation of a photonic circuit provides for the realization of a network of channels with tunable interaction (see for example [7]). Despite being an up-and-coming technology, the calibration of the network necessary before the quantum state measurement is still not trivial and opens issues. Specific tools for controlling or partially aiding the calibration in such structures are necessary.

Integrated photonic devices are generally subject to fabrication tolerances that make an *a priori* precise knowledge of the MZI network state impossible. As long as these tolerances manifest as unitary transformations themselves (typically phase fluctuations in virtually identical waveguides or coupling changes in the directional couplers), it is generally possible to calibrate the system and retrieve the desired configuration [9]. The calibration exploits the use of a relatively

Martino Bernard is with the Centre for Sensors and Devices, Fondazione Bruno Kessler, I-38123 Povo, Italy

Luca Gemma, Davide Brunelli are with the Department of Industrial Engineering, University of Trento, I-38123 Povo, Italy.

Corresponding author: luca.gemma@unitn.it

We acknowledge the support of the MNF Laboratory staff of FBK during sample fabrication. We acknowledge financial support from the Autonomous Province of Trento, under the initiative *"Quantum at Trento - Q@TN"*, projects *Q-PIXPAD* and *CoSiQuP*. This project has received funding from the European Union's Horizon 2020 research and innovation programme under grant agreements No 777222, ATTRACT *INPEQuT* and No 899368, *EPIQUS*.

This article has been accepted for publication in IEEE Journal on Emerging and Selected Topics in Circuits and Systems. This is the author's version which has not been fully edited and content may change prior to final publication. Citation information: DOI 10.1109/JETCAS.2022.3200937.

strong (10mW) laser to map the actual configuration state of the MZI net and to build a calibration table for each Degree of Freedom (DoF). Once the MZI has been calibrated with the bright coherent state, the knowledge of the MZI DoFs is then used to prepare the system to perform unitaries on quantum states of light. Similar systems with large nets of MZI are already on the market [7] and they need reliable calibration procedures.

This paper proposes an automatic tool with two main goals: (i) to estimate the light field intensity in any arbitrary point of the photonic circuit, and (ii) to achieve optimal system configuration without the need for bulk, invasive off- or on-chip detectors. Furthermore, we tested the entire tool chain on PICs that we fabricated in our facilities demonstrating its functionality. The main scientific contributions of this paper are described as follows:

i) we have developed an optical tool using Python and computer vision to non-invasively estimate the output intensities of light (infra-red laser) for each MZI at each stage of our Clements architecture;

ii) we have designed an optimization algorithm to inspect and find an optimal solution for maximizing or minimizing a specific output based solely on the output sensed on-chip through a digital multimeter;

iii) we have computed the theoretically expected output intensities and phases of an MZI in our chips to validate the experimental measurements further;

iv) we have performed several measurements on our fabricated PIC structures to test the goodness of our optical tool, thus being able to compare the estimated output of the image processing algorithm with the actual sensed one retrieved by our on-chip measurements;

v) we have also tested the optimization algorithm with the image processing information instead of the on-chip digital multimeter information.

The paper is structured as follows: in Section II, related works on photonic integrated chips are illustrated, and a short introduction is given. Section III illustrates the fabrication process. Section IV presents the image processing and the optimization algorithms, illustrating their main logic, and discusses the theoretic output of a single MZI to validate the experimental measurements retrieved on the whole Clements architecture. Section V illustrates how the two sets of measurements on our fabricated PIC were made. Section VI compares the on-chip measurements with the off-chip ones, illustrating the robustness and goodness of the image processing approach as a valid and viable solution for an automation tool. Finally, Section VII summarizes the results and concludes the paper by proposing future works.

II. Related Works

PICs are an appealing technology because of their CMOS compatible fabrication process, together with the possibility to use Silicon Nitride (SiN) and Silicon Oxynitride (SiON) waveguides, which are transparent in a wide band from the ultraviolet to the infrared region of the visible spectrum. SiN waveguides constitute the state-of-the-art in terms of on-chip losses for these chips [10], consolidating SiN materials as one of the most robust solutions for near-infrared architectures.

In addition, PICs have been proven to be valid for implementing essential quantum elements such as photonic switches, as described in [11], where the authors realized a photonic switch by a series of MZIs for simultaneously capturing data. The main elements embedded in our PICs are respectively the MZIs and the photon detectors. MZI is a more robust solution to simple beam splitters when dealing with light path modification between two adjacent waveguides; they are composed of a cascade of two beam splitters with two phase-shifters, achieving two degrees of freedom system, i.e., being able to control both the amplitude and the relative phase of the light passing through. For the PICs used in this work, we have previously characterized both the Ti-TiN thermistors used as phase shifters [12] and the silicon photodiodes used as photon detectors [13]; thus, it is now possible to perform a qualitative estimate of the output based on such characterizations. Two main architectures are established when realizing a forward network of interferometers that allow unitary transformations: the Reck and the Clements [14]. Reck et al. in [15] proved that a triangular configuration of 2x2 beam splitters and phase-shifters can achieve any arbitrary unitary transformation of the input channels. In addition to the possibility of reaching arbitrary unitary transformation, the Reck configuration offers a trivial mean of calibration for each element in the net, which emerges naturally from the triangular architecture. As the interest in such photonic circuits has considerably grown through the years, Clements et al. developed a more compact structure illustrated in [16]. It is of great importance to obtain efficient structures capable of arbitrary unitary transformations, such as the Reck or the Clements in the photonic case, as they represent a possible base building block for quantum computers. Using the same number of beam splitters as in a Reck configuration, Clements et al. got a notably shorter optical depth of the structure, thus considerably reducing both the footprint and the propagation losses at the cost of a non-trivial calibration of the system components. The two MZI networks (Reck and Clements) are illustrated in Fig. 1: the triangular and the symmetric layouts typical of the Reck and Clements architectures respectively can be noticed. In addition, also the base building block of the PIC, the MZI, is illustrated, featuring the two phase shifters (θ and ϕ) and introducing the coupling coefficient k of the beam splitters and the transmission coefficient t later mentioned in Section IV.

Finally, image processing techniques are widely used for fiber optics, as inspection methods to detect defects like in [17] where the authors developed a system robust to different gains and exposures, or for adjusting the correct alignments like in [18]. Few works also exist which imply optical inspection of camera images for extracting the performances of a PIC, such as in [19], where the Mashanovich et al. used a long wave infrared camera to evaluate the performance of Mid-Infrared Germanium-based photonic devices, computing the propagation losses per unit length of the waveguides. Nevertheless, to our knowledge, there are still no works in literature proposing visual tools to optimize or tune the output of a PIC-based on

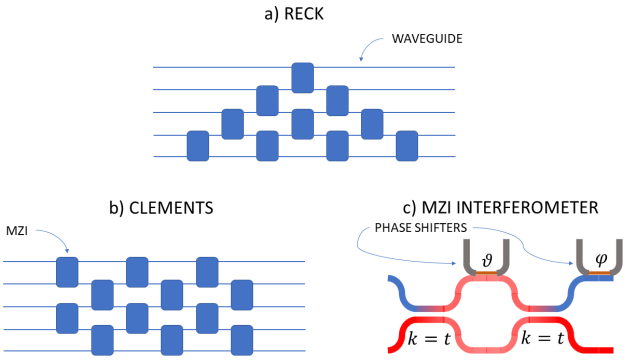

Fig. 1. Reck (a) and Clements (b) architectures along with the PIC building block, the MZI interferometer (c).

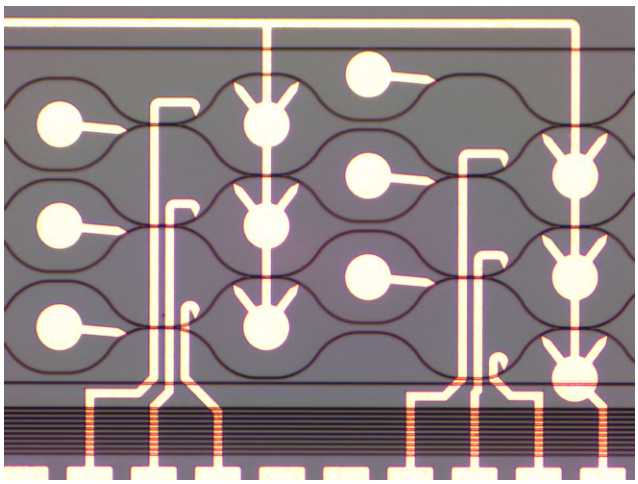

Fig. 2. Optical micrograph of the PIC in the region of the MZI network. In the images the waveguides are the wavy lines from left to right.

computer vision. Thus, one of the major contributions of this work is to fill this gap by presenting and discussing a custom computer vision-based solution to estimate the state (i.e., the configuration) of a photonic chip by exploiting scattering at the surface of the waveguides without the need of dedicated output detectors. Our method is a robust solution which can be embedded in an automation tool to quicken the design and tuning of PIC systems without the need for invasive on-chip probes and detectors.

III. Device Fabrication

We fabricated a photonic integrated circuit consisting of a net of waveguides interacting through tunable MZIs. The tunability is obtained by embedding thermistors as phase shifters. The interferometers are arranged in a Clements architecture [16], featuring six inputs and six outputs. The chips were fabricated in the clean-room of the Sensors and Devices facility of the Bruno Kessler Foundation (FBK) [20].

The chips have been fabricated starting from an epitaxial growth of silicon on a crystalline silicon wafer with a 150 mm diameter. The fabrication process starts with the realization of the silicon electronics, i.e., the photodiodes, in the epitaxial layer by ion implantation. Then, the substrate is covered with an oxide cladding that is shaped in a shallow edge through wet-etching technique [21] in the detector region to allow for localized waveguide-detector coupling.

The photonic layer is realized with the deposition of Silicon Oxynitride SiON thorough Plasma Enhanced Chemical Vapour Deposition technique, which is then patterned into waveguides through i-line lithography and reactive ion etching. The waveguides are then encapsulated into a silicon oxide layer deposited with Low-Pressure Chemical Vapour Deposition from Boro-Phospho-Silicate Glass (BPSG) and Tetraethoxysilane precursor (TEOS). The oxide layer protects the waveguide from the outside environment and provides optical insulation from the metals that are deposited on top of the chip to realize the thermistors. The thermistors are realized with a multi-stack layer of Titanium-Titanium Nitride and Titanium (Ti-TiN-Ti). An additional thick layer of aluminum is then deposited to realize via contacts towards the underneath detectors and highly conductive lines toward the device's pads. Finally, the wafer is diced into chips packaged on appositely designed Printed Circuit Boards (PCBs). The chip is then connected to the PCB via ball-wire-bonding and interfaced with the characterization and control setup.

A more detailed description of the fabrication process is presented in [22]. The final system contains 27 thermistors distributed on 10 MZIs, thus bearing a 27 DoFs system. In Fig. 2 the MZI layout can be appreciated, with waveguides in black and metallic pads and routing in white.

IV. Methods

We developed an optical tool to retrieve through camera images the light intensities of custom regions on the PIC. Moreover, we defined an optimization algorithm to maximize either the single output current of the integrated detector measured with a Keithley source-meter or all the measured intensities retrieved by the image processing tool. Python version 3.9.12 was used throughout the entire work. Qontrol library was used to interface with the Q8b driver model. We configured four drivers, allowing us to control up to 32 channels. Through a custom interposer, each channel is then connected to a Ti-TiN thermistor embedded in the substrate of the PIC, allowing to heat the corresponding zone of the overlapped waveguide locally, thus changing the refractive index and, in turn, the light (laser) path.

A 2450 Keithley digital multimeter is connected to one of the output lines of our chip; thus, we used the PyVisa package to interface with the instrument, configure it, and perform each measurement. The wx packag e [23] was used to take a custom screenshot of the live stream of our Thorlabs camera [24]. The Opencv cv2 computer vision library [25] was used to perform all the required image processing tasks. First, the image corresponding to the currently taken screenshot is displayed; then, using events and the HighGUI callback function for when a mouse event occurs (setMouseCallback()), the user can select a custom number of rectangle regions where the sums of all the inner pixel values are computed. This allows to gather information about the scattered light intensities in such regions.

In addition, to compensate for different light conditions among different taken screenshots throughout the entire experiment run, a background "dark" region where there are no waveguides or other active elements is selected, and the inner pixel values sum is computed similarly. Then, the background value is subtracted from every analyzed region. For more consistent data and to avoid normalization issues, the size of the first rectangle region is registered, and each subsequent rectangle is made with the same dimensions so that the total signal comes from the contribution of the same number of pixels for each selected region. This method was chosen considering mostly straight waveguides that thus provide approximately the same amount of scattering signal in the fixed shape integration region.

The output target vector is specified as an n-element unitary vector. In the case of this experiment, its components will be 1 for a chosen output and 0 for all other outputs. The vector of the computed measurements (i.e. the sums of inner pixel values normalized on the number of pixels) is then normalized globally to be constrained to a unitary norm, thus making it comparable with the target vector.

Secondly, an optimization algorithm was developed to maximize the output sensed by either the image processing algorithm or the digital multimeter. The working logic is straightforward:
i) a voltage sweep is performed on each channel from a start value to a stop value with a custom step (usually respectively 0 V, 12 V, and 0.5 V);
ii) during the sweep, the evolution of the system state is then acquired with either the multimeter, measuring the corresponding current reading of a single output, or through image processing acquiring the scattering intensity in all the defined regions;
iii) for each DoF sweep, the values corresponding to the minimum of the cost function as well as the driving voltages and current of each TiTiN thermistor are stored in a proper structure (i.e., each degree of freedom);
iv) after each sweep, the last analyzed DoF is set in the configuration, which held the minimum of the cost function over that sweep, and then the algorithm proceeds with a sweep over the next DoF.

To achieve a more robust algorithm and avoid local minima of the cost function, the order of inspected channels is randomized, and the search is repeated for a custom number of tries. At each step, the configuration is saved in an ASCII file, and a capture of the Thorlabs camera stream view is taken and linked to the saved configuration through a univocal ID-generated number; this grants full availability of all the retrieved data for future off-line processing. The trend of light intensity within each region is computed, stored in proper structures, and displayed. For the image processing, the optimization criterion minimizes the output of a cost function defined as the norm of the difference between the measured and the expected output vector. Conversely, for the Keithley-based algorithm, the optimization criterion seeks the maximum of the current readings for the target output.

The optimization algorithm in the case of captured images from the Thorlabs camera is illustrated below. First, for every selected region (i.e. output), the sum of all the pixel intensities $s_i(x, y)$ is divided by the region's area A_{R_n}, and then the background offset B is subtracted:

$$S_n = \frac{\sum_{i \in R_n} s_i(x,y)}{A_{R_n}} - B$$

where the background offset is computed as the sum of all the pixel intensities $s_i(x, y)$ in its region divided by the respective region's area A_B

$$B = \frac{\sum_{i \in B} s_i(x,y)}{A_B}$$

then the region vector S is built as

$$S = (S_1, S_2, \cdots, S_n)$$

and then normalized to unitary norm

$$S_{i\text{normalized}} = \frac{S_i}{\sum_{i \in B}(\sqrt{S_i^2})} \qquad \forall S_i$$

The output ΔS of the cost function is then built as

$$\Delta S = \sum_{i=1}^{n} (\sqrt{(S_{i\text{normalized}} - T_i)^2})$$

where

$$T = (T_1, T_2, \cdots, T_n), \qquad \sum_i T_i^2 = 1$$

is the expected target output vector, which, in case of maximizing the k-th output and minimizing the remaining is equal to

$$\begin{cases} T_i = 1 & \text{for i = k} \\ T_i = 0 & \text{for i} \neq \text{k} \end{cases}$$

then the optimal value of S (and, in turn, the optimal thermistor drive voltage configuration) is when ΔS is minimized.

Moreover, we aimed at obtaining a compact formula for the output of a single MZI and for a complete Clements architecture. As a matter of fact, by having an explicit expression of such elements, it would be possible to simulate the output and compare them to the measured ones. In a MZI, the tuning is made through the thermo-optic effect. The optical path which is the product nL of the refractive index n and the geometrical path L, is thus changed by changing the refractive index:

$$nL = ({n_{\text{eff}}}^0 + \frac{dn_{\text{eff}}}{dT} + \Delta T)L$$

where ${n_{\text{eff}}}^0$ is the refractive index at room temperature, $\frac{dn_{\text{eff}}}{dT}$ is the thermo-optic coefficient and ΔT is the temperature variation with respect to the room temperature. Acting on the phase-shifters allows for changing the phase accumulated by the photons in the heated region in between two coupling regions, leading to a control of the interference pattern. In matrix form, the output for a single beam splitter can be written as:

$$\begin{pmatrix} O_1 \\ O_2 \end{pmatrix} = \begin{pmatrix} I_1 \\ I_2 \end{pmatrix} \begin{bmatrix} t & ik \\ ik & t \end{bmatrix}$$

where k the coupling coefficient of the beam splitter and $t = \sqrt{1 - |k|^2}$ is the transmission coefficient. The equations for an

MZI, realized with a cascade of two beam-splitters separated by a free-propagation tract, can be written as:

$$\begin{pmatrix} O_1 \\ O_2 \end{pmatrix} = \begin{pmatrix} I_1 \\ I_2 \end{pmatrix} [M_1] [M_2] [M_3]$$

where

$$M_1 = \begin{bmatrix} \sqrt{(1-|k_1|^2)} & ik_1 \\ ik_1 & \sqrt{(1-|k_1|^2)} \end{bmatrix}$$

$$M_2 = \begin{bmatrix} e^{i\phi_1} & 0 \\ 0 & e^{i\phi_2} \end{bmatrix} M_3 = \begin{bmatrix} \sqrt{(1-|k_2|^2)} & ik_2 \\ ik_2 & \sqrt{(1-|k_2|^2)} \end{bmatrix}$$

which, in the case of identical beam splitters ($k_1 = k_2$), leads to

$$\begin{pmatrix} O_1 \\ O_2 \end{pmatrix} = \begin{bmatrix} -e^{i\phi_2}k^2 + e^{i\phi_1}t^2 & ie^{i\phi_1}kt + ie^{i\phi_2}kt \\ ie^{i\phi_1}kt + ie^{i\phi_2}kt & -e^{i\phi_1}k^2 + e^{i\phi_2}t^2 \end{bmatrix} \begin{pmatrix} I_1 \\ I_2 \end{pmatrix}$$

where ϕ_1, ϕ_2 are the phases of each beam splitter arm and k and t are an inner parameters for the phase shifters. By making the following assumptions on the parameters above:

$$\begin{cases} \phi_2 = \phi_1 + \theta \\ \phi_1 = 2\pi n_{\text{eff}} \frac{L}{\lambda} \end{cases} .$$

where θ is the relative phase-shift of one phase w.r.t. the other. The analytic expression for the two outputs can be derived as:

$$\begin{pmatrix} O_1 \\ O_2 \end{pmatrix} = \frac{1}{2} \begin{pmatrix} e^{i\phi_1}(1-e^{i\theta}) \\ ie^{i\phi_1}(1+e^{i\theta}) \end{pmatrix}$$

Similarly, the expression for a Clements architecture with an arbitrary number of outputs can be obtained. The theoretical outputs plot of a single MZI obtained through the matrices illustrated above is reported in Fig. 3, showing the two normalized outputs (output 1 in blue and output 2 in orange), which complementary increase and decrease as the split ratio changes in response to a change in θ. The corresponding experimental measured outputs are illustrated in Fig. 4. On top, the I-V curves (in mA and V) for a triangular voltage sweep from 0 to 12V of the phase shifters are shown, depicting a roughly linear trend, with under-linear behaviour for regions near the maximum voltages, as in such areas, the thermoresistive effect becomes more relevant. On the bottom, the voltage readings in mV for the same voltage sweep are depicted, showing curves similar to the theoretical ones of Fig. 3.

It is worth noting that the curves do not cover a full period of the sinusoidal; this is due to the maximum cap of 12V, which, along with the 10 mA current compliance, was imposed to limit the power dissipated over each thermistor and avoid breakage as already discussed in [12]. This is not a fundamental limit and heaters with better thermo-optic responsivity and higher current tolerance have already been fabricated in the next-generation devices [26] The effects of controlling a single MZI are shown in Fig. 5 where the split ratio is controlled and changed from roughly 50:50 to a full transfer to the lower output, exactly as reported in Fig. 4. Moreover, for the sake of clarity, the effects of controlling multiple MZIs for the whole Clements structure are shown in Fig. 6, where from an almost evenly distributed input visible

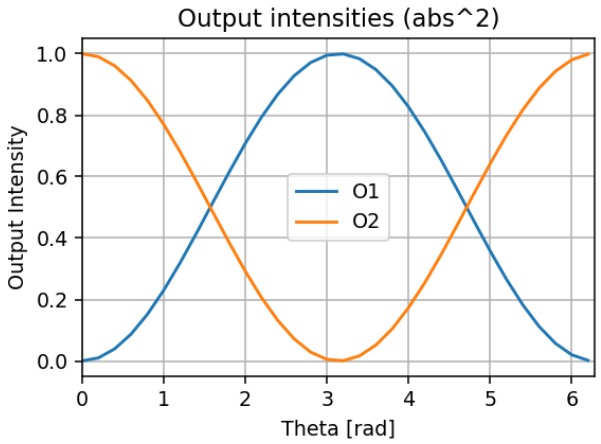

Fig. 3. Theoretical output of a single MZI computed through the transformation matrices described in this section.

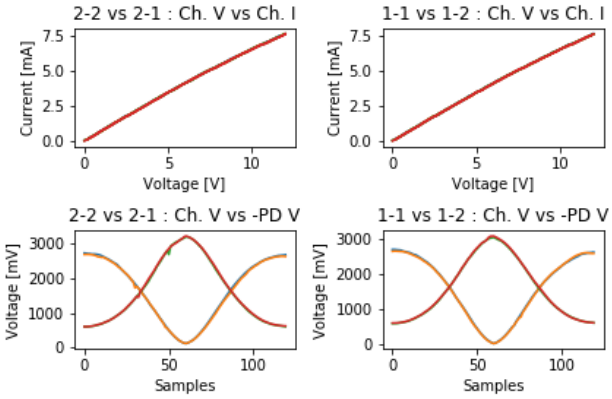

Fig. 4. Experimental outputs of a single MZI for input 2 (left) and input 1 (right). I-V curves for controlled TiTiN thermistors (top) and voltage readings in mV for the two outputs (bottom). It is worth noting the similarities with Fig. 3

throughout all the architecture (top), a single branch is selected (bottom), as further detailed in Section VI.

V. Measurements

All the measurements were performed on a Silicon Nitride PIC wire bonded to a PCB board. The wire-bonding is necessary to contact the silicon photodiodes output detectors available for all the six output branches of our Clements architecture, and the 27 TiTiN phase-shifter thermistors act as our degrees of freedom. Fig. 7 shows the measurement setup. We injected an 850 nm wavelength infrared-laser beam through a target input waveguide among all the six available ones and ran the optimization algorithm aiming to maximize a target output. In order to validate our optical tool, we produced two sets of measurements for the same optimization goal, one using a classical approach of on-chip sensing and one relying solely on live-streamed images. The two sets were produced as follows:

i) the first set with a 2450 Keithley digital multimeter acquiring the photocurrent from the output detector of the target output to be maximized

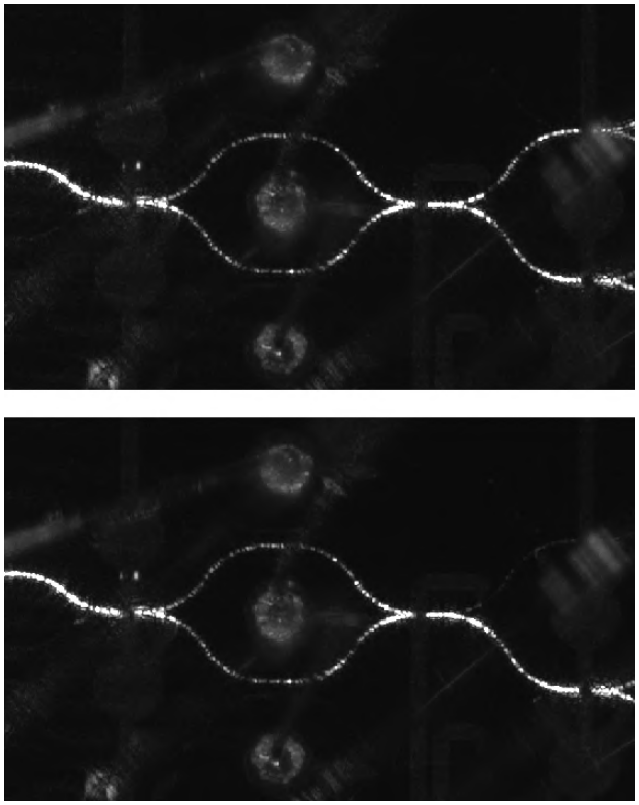

Fig. 5. Single MZI actuation. The rest state (top) has the output intensities about equally distributed. By actuating the thermistor on one of the two arms of the MZI it is possible to change the phase and reach an interference condition where all of the light intensity is directed towards output 2 (bottom).

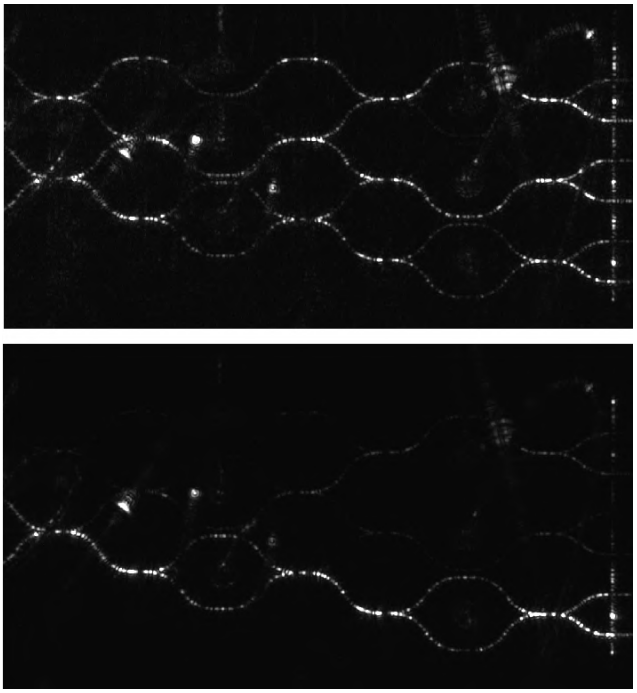

Fig. 6. Effect of controlling multiple MZIs in a Clements architecture: the system starts in the rest configuration (top) where the light distributes among the channels. With the optimization algorithm the phase in each MZI is changed until almost all light is driven in the target output (bottom).

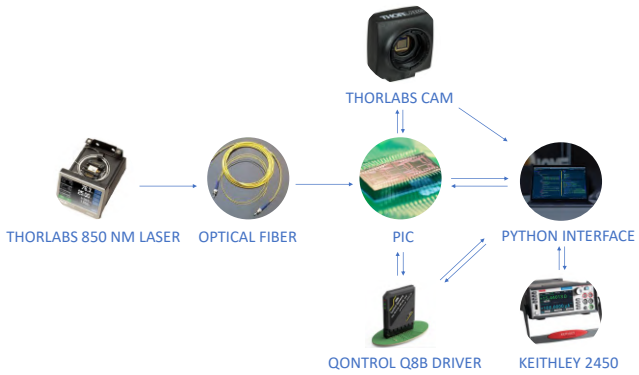

Fig. 7. Lab setup for measurements.

ii) a second set with the image processing algorithm running to maximize a target output vector configuration. The first set was produced by working in the reverse polarization region for the photodiodes, polarizing them at -3V, such as in [13]. The phase-shifters were voltage-driven one after the other through a voltage sweep from 0 to 12V with a discrete step of 0.5V. The output was sensed through the relative output detector through the 2450 Keithley digital multimeter and acquired with Python exploiting the PyVisa library. This routine was repeated for different input-output configurations, selecting only the relevant set of degrees of freedom which would have an impact on the change of the optical path (as, for design, some DoFs do not contribute to each input/output combinations) to reduce the overall run time for the optimization algorithm. For the sake of consistency, the second set was produced by inspecting the same configurations of input-output used for the first set, running the optimization algorithm with the image processing, and extracting the output state estimation via visual information on the captured video live stream of the Thorlabs camera mounted on the microscope, which senses the intensity in the waveguides by imaging the scattering on the surface. By using this approach and not being limited to the wire-bonded detectors, we set a complete output vector as our target, thus being able to maximize one output and minimize the remaining ones simultaneously. To avoid saturation and loss of resolution, we adjusted the gain on the captured image between each measurement.

VI. Results

As illustrated in V we performed two sets of measurements to test the optimization algorithm: i) one accessing the current measurements coming from the Keithley digital multimeter when reverse biasing the silicon photodetector corresponding to the output to be maximized (Figures 8 and 10) and ii) one using the image processing algorithm to set all the outputs to a specific target vector, thus allowing for simultaneous optimization of all the outputs (Figures 9 and 11).

It is worth considering that although looking for the maximum of a specific output, the Keithley sensed current plot produced by the optimization algorithm looks for minimizing the value as the diode is reverse biased, as the measurements have been registered in the inverse polarization region. First,

we started with an experiment injecting in input 3 and targeting output 2. In Fig. 8, the infra-red laser beam was injected into input 3 of the Clements architecture, and six degrees of freedom (thermistors acting as phase-shifters) were investigated during the search for the optimal voltage drive configuration to drive the maximum amount of the light in the target output waveguide.

The third panel of Fig. 8, shows the sensed current as a function of the sweep-step exploration. Notice that the information provided by each thermistor's sweep was taken into account, exploring each DoF full range and setting the DoF current as the optimal current reached at the minimum value during each sweep (visible in the plot: after each sweep, i.e. each V-shaped curve, the temporary optimal value was set as the lowest value reached). Moreover, comparing the first (start, from random configuration) and last (end, optimized configuration) point in the graph, we can notice that the current increased five-fold. This fact is further confirmed by looking at the images before (top-left) and after (top-right) the optimization. An analogous experiment was conducted by reaching the same target configuration, starting from the same input, and using the scattering intensity as the feedback for the optimization. This method, reported in Fig. 9, obtained similar results in terms of light-routing, as shown in the captured images on top, to be compared with the analogous images from Fig. 8.

By looking at the plot of the averaged detected pixel intensities for the six outputs, the optimization steps are clearly visible: the output 2 (orange line), which had to be maximized, is progressively increasing up to a maximum which is more than three times higher than the starting value and the other outputs, which instead had to be minimized, drop to values close to zero.

It is worth noting that, as the reported values are the ones compensated by the background offset (i.e., the difference between the averaged pixel values in the region identified as background and the one identified as the output), the results can also be negative. An improved "dark subtraction" taking into account the local nature of the background could improve the algorithm in the future. Another interesting phenomenon worth noting is the correlation between different output trends during optimization: several outputs present either positive or negative correlation due to the dependence of two or more outputs to a specific degree of freedom, especially to the degrees of freedom closer to the input. This phenomenon is, for example, clearly visible when looking at output 1 (blue line) and output 2 (orange line) between image numbers 0 and 50, which corresponds to the degree of freedom of the last beam splitter, which can theoretically produce an arbitrary split ratio between the two outputs.

Secondly, another set of input-output (and consequently also degrees of freedom) has been reported in Fig. 10 for the Keithley algorithm and Fig. 11 for the image processing algorithm. Fig. 10 shows the effect of the Keithley optimization algorithm when the laser beam is injected into input 4 and the output to be maximized is the sixth.

Similarly to Fig. 8, the maximization (minimization) trend is clearly visible, with only two degrees of freedom not contributing significantly to the optimization search and the remaining seven greatly changing the output. Again, the effectiveness of the optimization procedure is confirmed after each thermistor's sweep. The temporary optimal value is updated to the minimum reached during the sweep. Finally, the same experimental conditions have been replicated with the image processing optimization algorithm, and the results are illustrated in Fig. 11: for input 4 and the same nine thermistors controlled, the target output vector implied output 6 (brown line) to be maximized and all other ones to be minimized.

As noticeable in the plot, output 6 has been correctly maximized, increasing by roughly 100% the averaged pixel intensity while correctly minimizing the pixel intensity of the other regions. Again, it is worth noting that since output 6 (brown line) and output 5 (purple line) lie after the same last beam splitter, their output patterns follow a similar trend up to the point where the degree of freedom corresponding to the common beam splitter is inspected (between image number 100 and 150), at which point the trend is almost the opposite, confirming the inspection of the splitting ratio between the two outputs.

In conclusion, also for this configuration, the Keithley measures validated the image-processing-based optimization method, which is confirmed to be effective in searching for a maximum (minimum).

Being able to get optimization results as good as (or even better than) the ones achieved through classical approaches based on on-chip sensing (with silicon photodiodes) allows diminishing the number of sensors embedded in the chip, thus increasing the maximum available space for circuit design and reduce the routing complexity. This is especially important when the detectors at the end of the circuit are designed to operate at the single photon regime because they are not suited to be used during the calibration routine. Moreover, it is also worth considering that this optical tool can be used to select other different regions of the PIC and is not only limited to the outputs of the entire architecture (be it a Clements one, a Reck one or any other configuration). Thus the proposed method can inspect and tune arbitrary points even in the inner region of the circuit, which are usually not accessible via monitor photodiodes. Finally, the algorithm can be easily re-implemented, and this tool can be extended to operate not only to Clements architectures, but also to Reck or any other ones, as it does not rely on specific formulas or inner logic typical of a specific architecture.

VII. Conclusions

This paper presents a solution for tuning the output of a photonic integrated circuit architecture through processing live-stream images from a Thorlabs camera through computer vision. The method has been validated using a digital multimeter and inverse polarizing silicon photodiodes as output detectors. This approach proved to be effective when maximizing a single output with the image processing algorithm extending the capabilities of the optimization algorithm from a single output to a complete output target configuration. This proposed tool can potentially be a highly beneficial solution

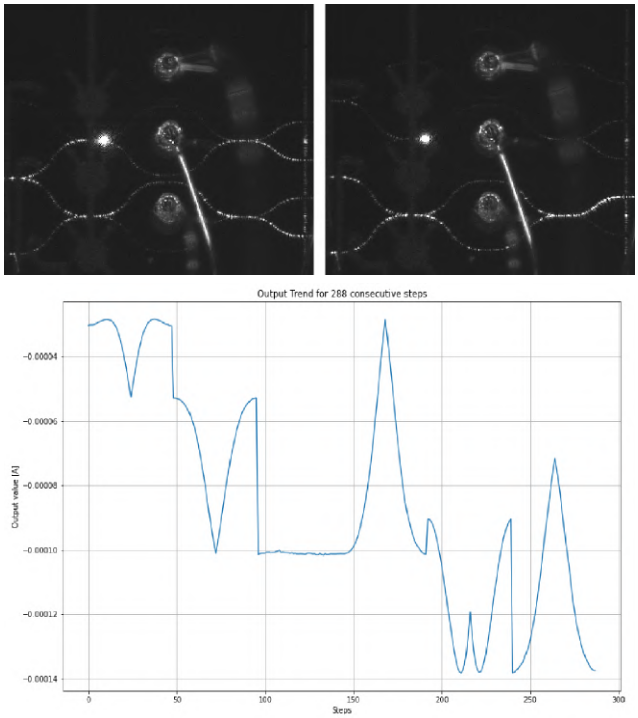

Fig. 8. Optimization results with Keithley algorithm with input 3 and output 2. Captured images before (top-left) and after (top-right). Sensed current trend in reverse bias during optimization (bottom).

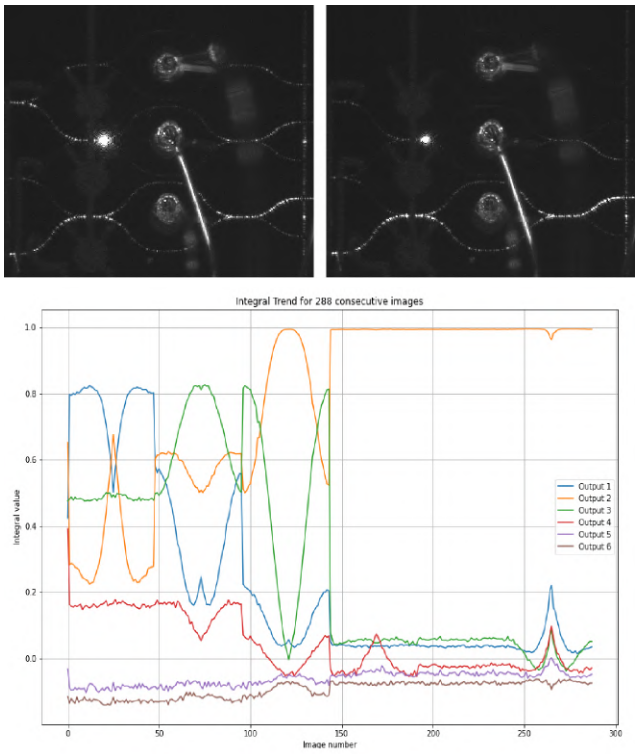

Fig. 9. Optimization results with Image Processing algorithm with input 3 and output 2. Captured images before (top-left) and after (top-right). Detected pixel intensity during optimization (bottom).

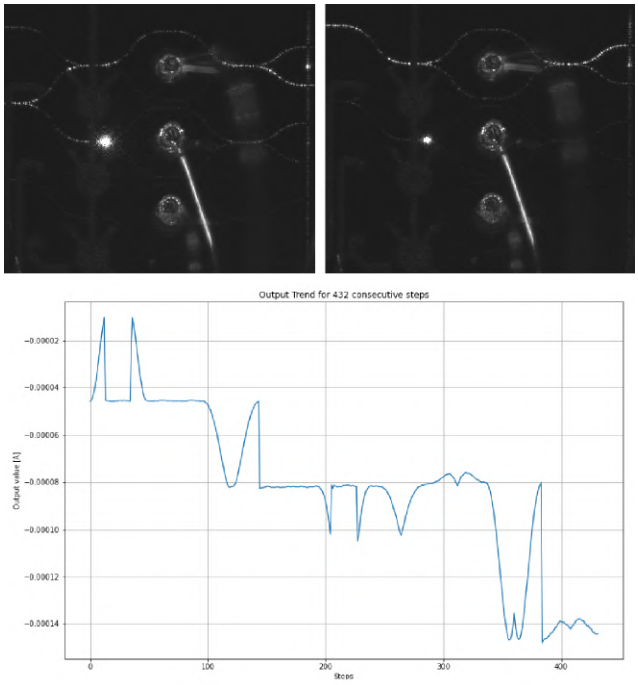

Fig. 10. Optimization results with Keithley algorithm with input 4 and output 6. Captured images before (top-left) and after (top-right). Sensed current trend in reverse bias during optimization (bottom).

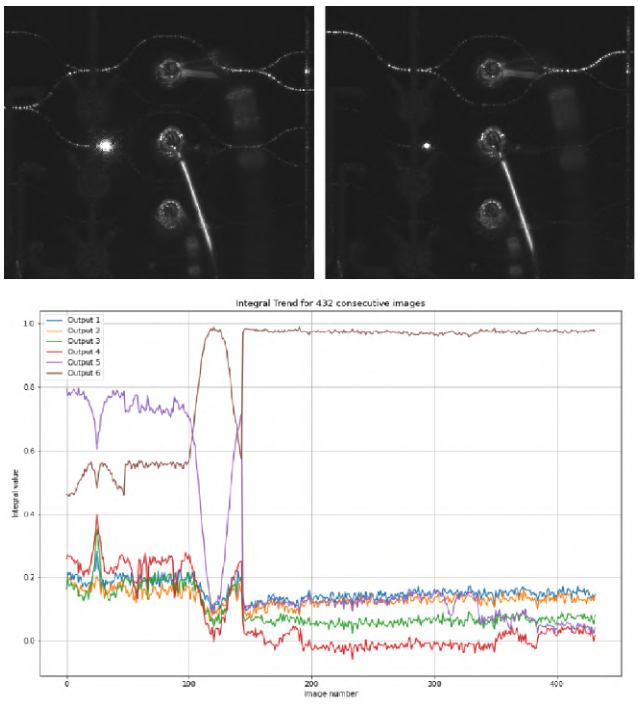

Fig. 11. Optimization results with Image Processing algorithm with input 4 and output 6. Captured images before (top-left) and after (top-right). Detected pixel intensity during optimization (bottom).

for quantum photonics circuit configuration. It eliminates the need for multiple fixed on-chip monitor detectors and enables an arbitrary optimization for any area of the PIC, even for the middle "in-between MZIs" regions. Future works will consider the relevance of the order of inspection of the degrees of freedom during the optimization search. We will embed the algorithm in a design automation tool that automatically detects the best order for propagating the optimization schedule. Moreover, the tool will promote what degrees of freedom can significantly contribute to the maximization/minimization procedure. Eventually, we will do a performance comparison between chips with embedded output detectors (such as the one used in this work) and others with off-chip detectors to improve the inspection of chip detectors' efficiency.

REFERENCES

[1] W. O'Brien, M. Vahidpour, J. T. Whyland, J. Angeles, J. Marshall, D. Scarabelli, G. Crossman, K. Yadav, Y. Mohan, C. Bui *et al.*, "Superconducting caps for quantum integrated circuits," *arXiv*, 2017. [Online]. Available: https://arxiv.org/abs/1708.02219

[2] Y. Liu, Z. Minev, T. McConkey, and J. Gambetta, "Design of interacting superconducting quantum circuits with quasi-lumped models," *Bulletin of the American Physical Society*, 2022.

[3] S. Vaitiekėnas, G. W. Winkler, B. van Heck, T. Karzig, M.-T. Deng, K. Flensberg, L. I. Glazman, C. Nayak, P. Krogstrup, R. M. Lutchyn *et al.*, "Flux-induced topological superconductivity in full-shell nanowires," *Science*, vol. 367, no. 6485, p. eaav3392, 2020.

[4] I. H. Kim, Y.-H. Liu, S. Pallister, W. Pol, S. Roberts, and E. Lee, "Fault-tolerant resource estimate for quantum chemical simulations: Case study on li-ion battery electrolyte molecules," *Physical Review Research*, vol. 4, no. 2, p. 023019, 2022.

[5] R. Blümel, N. Grzesiak, N. H. Nguyen, A. M. Green, M. Li, A. Maksymov, N. M. Linke, and Y. Nam, "Efficient stabilized two-qubit gates on a trapped-ion quantum computer," *Physical Review Letters*, vol. 126, no. 22, jun 2021.

[6] K. Boothby, C. Enderud, T. Lanting, R. Molavi, N. Tsai, M. H. Volkmann, F. Altomare, M. H. Amin, M. Babcock, A. J. Berkley *et al.*, "Architectural considerations in the design of a third-generation superconducting quantum annealing processor," *arXiv*, 2021. [Online]. Available: https://arxiv.org/abs/2108.02322

[7] C. Taballione, M. C. Anguita, M. de Goede, P. Venderbosch, B. Kassenberg, H. Snijders, N. Kannan, D. Smith, J. P. Epping, R. van der Meer *et al.*, "20-mode universal quantum photonic processor," *arXiv*, 2022. [Online]. Available: https://arxiv.org/abs/2203.01801

[8] M. Schuld and N. Killoran, "Is quantum advantage the right goal for quantum machine learning?" *arXiv preprint*, 2022. [Online]. Available: https://arxiv.org/abs/2203.01340

[9] D. A. B. Miller, "Perfect optics with imperfect components," *Optica*, vol. 2, no. 8, pp. 747–750, 2015.

[10] C. G. H. Roeloffzen, M. Hoekman, E. J. Klein, L. S. Wevers, R. B. Timens, D. Marchenko, D. Geskus, R. Dekker, A. Alippi, R. Grootjans *et al.*, "Low-loss si3n4 triplex optical waveguides: Technology and applications overview," *IEEE Journal of Selected Topics in Quantum Electronics*, vol. 24, no. 4, pp. 1–21, July 2018.

[11] A. Annoni, E. Guglielmi, M. Carminati, S. Grillanda, P. Ciccarella, G. Ferrari, M. Sorel, M. J. Strain, M. Sampietro, A. Melloni *et al.*, "Automated routing and control of silicon photonic switch fabrics," *IEEE Journal of Selected Topics in Quantum Electronics*, vol. 22, no. 6, pp. 169–176, Nov 2016.

[12] L. Gemma, M. Bernard, M. Ghulinyan, and D. Brunelli, "Analysis of control and sensing interfaces in a photonic integrated chip solution for quantum computing," in *Proceedings of the 17th ACM International Conference on Computing Frontiers*, ser. CF '20. New York, NY, USA: Association for Computing Machinery, 2020, p. 245–248. [Online]. Available: https://doi.org/10.1145/3387902.3394034

[13] L. Gemma, M. Bernard, M. Ghulinyan, and D. Brunelli, "Analysis of photodiode sensing devices in a photonic integrated chip solution for quantum computing," in *2020 IEEE SENSORS*. IEEE, 2020, pp. 1–4.

[14] D. Pérez, I. Gasulla, P. D. Mahapatra, and J. Capmany, "Principles, fundamentals, and applications of programmable integrated photonics," *Adv. Opt. Photon.*, vol. 12, no. 3, pp. 709–786, Sep 2020.

[15] M. Reck, A. Zeilinger, H. J. Bernstein, and P. Bertani, "Experimental realization of any discrete unitary operator," *Phys. Rev. Lett.*, vol. 73, pp. 58–61, Jul 1994.

[16] W. R. Clements, P. C. Humphreys, B. J. Metcalf, W. S. Kolthammer, and I. A. Walmsley, "Optimal design for universal multiport interferometers," *Optica*, vol. 3, no. 12, pp. 1460–1465, Dec 2016.

[17] N. Vahabi, D. Yang, and D. R. Selviah, "Improving data transmission in fiber optics by detecting scratches on the fiber end face," in *2018 IEEE British and Irish Conference on Optics and Photonics (BICOP)*, 2018, pp. 1–4.

[18] A. A. Samad and C. Unni, "Image processing based end-view alignment for symmetric specialty optical fibers," in *2018 Second International Conference on Inventive Communication and Computational Technologies (ICICCT)*, 2018, pp. 1080–1082.

[19] G. Mashanovich, C. Mitchell, J. Soler Penades, A. Khokhar, C. Littlejohns, W. Cao, Z. Qu, S. Stankovic, F. Gardes, T. Ben Masaud *et al.*, "Germanium mid-infrared photonic devices," *Journal of Lightwave Technology*, vol. PP, pp. 1–1, 11 2016.

[20] Sensor and devices, fondazione bruno kessler. [Online]. Available: https://sd.fbk.eu/en/about-us/

[21] M. Ghulinyan, M. Bernard, R. Bartali, and G. Pucker, "Formation of mach angle profiles during wet etching of silica and silicon nitride materials," *Applied Surface Science*, vol. 359, pp. 679–686, 2015.

[22] M. Bernard, F. Acerbi, G. Paternoster, G. Piccoli, L. Gemma, D. Brunelli, A. Gola, G. Pucker, L. Pancheri, and M. Ghulinyan, "Top-down convergence of near-infrared photonics with silicon substrate-integrated electronics," *Optica*, vol. 8, no. 11, p. 1363, 2021. [Online]. Available: https://www.osapublishing.org/abstract.cfm?URI=optica-8-11-1363

[23] wxPython Team. wxpython downloads. [Online]. Available: https://wxpython.org/pages/downloads/index.html

[24] T. Inc. Microscopy cameras. [Online]. Available: https://www.thorlabs.com/navigation.cfm?guide_id=2365

[25] OpenCV. Opencv-python tutorials. [Online]. Available: https://docs.opencv.org/4.x/d6/d00/tutorial_py_root.html

[26] G. Piccoli, "A silicon oxynitride platform for linear and nonlinear NIR photonics," vol. Conference 12148: Integrated Photonics Platforms II. SPIE, 2022, pp. Paper 12 148–13.